Research Square

Preprints are preliminary reports that have not undergone peer review.
They should not be considered conclusive, used to inform clinical practice,
or referenced by the media as validated information.

Electronic and magnetic excitations in La3Ni2O7

Ke-Jin Zhou

kejin.zhou@diamond.ac.uk

Diamond Light Source https://orcid.org/0000-0001-9293-0595

Xiaoyang Chen

State Key Laboratory of Surface Physics, Department of Physics, and Advanced Materials Laboratory, Fudan University

Jaewon Choi

Diamond Light Source

Zhicheng Jiang

Univerisity of Science and Technology of China https://orcid.org/0000-0001-7407-1176

Jiong Mei

Beijing National Laboratory for Condensed Matter Physics and Institute of Physics, Chinese Academy of Sciences

Kun Jiang

Institute of Physics, Chinese Academy of Sciences https://orcid.org/0000-0003-1136-2472

Jie Li

Nanjing University

S. Agrestini

Diamond Light Source https://orcid.org/0000-0002-3625-880X

Mirian Garcia-Fernandez

Diamond Light Source https://orcid.org/0000-0002-6982-9066

Hualei Sun

School of Physics, Sun Yat-Sen University

Xing Huang

Guangdong Provincial Key Laboratory of Magnetoelectric Physics and Devices, School of Physics, Sun Yat-Sen University

Dawei Shen

University of Science and Technology of China https://orcid.org/0000-0003-2402-7956

Meng Wang

School of Physics, Sun Yat-Sen University https://orcid.org/0000-0002-8232-2331

Jiangping Hu

Institute of Physics, Chinese Academy of Sciences https://orcid.org/0000-0002-4837-7742

Yi Lu

Nanjing University

Donglai Feng

USTC https://orcid.org/0000-0001-9370-5357

Physical Sciences - Article

Keywords:

Posted Date: March 5th, 2024

DOI: https://doi.org/10.21203/rs.3.rs-3901266/v1

License: This work is licensed under a Creative Commons Attribution 4.0 International License.
Read Full License

Additional Declarations: There is **NO** Competing Interest.

Electronic and magnetic excitations in $La_3Ni_2O_7$

Xiaoyang Chen,[1,*] Jaewon Choi,[2,*] Zhicheng Jiang,[3] Jiong Mei,[4,5] Kun Jiang,[4,5] Jie Li,[6] Stefano Agrestini,[2] Mirian Garcia-Fernandez,[2] Hualei Sun,[7] Xing Huang,[8] Dawei Shen,[3] Meng Wang,[8] Jiangping Hu,[4,9] Yi Lu,[6,10,†] Ke-Jin Zhou,[2,‡] and Donglai Feng[3,1,11,10,§]

[1]*State Key Laboratory of Surface Physics, Department of Physics, and Advanced Materials Laboratory, Fudan University, Shanghai 200438, China*
[2]*Diamond Light Source, Harwell Campus, Didcot OX11 0DE, UK*
[3]*National Synchrotron Radiation Laboratory and School of Nuclear Science and Technology, University of Science and Technology of China, Hefei, 230026, China*
[4]*Beijing National Laboratory for Condensed Matter Physics and Institute of Physics, Chinese Academy of Sciences, Beijing 100190, China*
[5]*School of Physical Sciences, University of Chinese Academy of Sciences, Beijing 100190, China*
[6]*National Laboratory of Solid State Microstructures and Department of Physics, Nanjing University, Nanjing 210093, China*
[7]*School of Science, Sun Yat-Sen University, Shenzhen, Guangdong 518107, China*
[8]*Guangdong Provincial Key Laboratory of Magnetoelectric Physics and Devices, School of Physics, Sun Yat-Sen University, Guangzhou, Guangdong 510275, China*
[9]*New Cornerstone Science Laboratory, Beijing, 100190, China*
[10]*Collaborative Innovation Center of Advanced Microstructures, Nanjing, 210093, China*
[11]*New Cornerstone Science Laboratory, University of Science and Technology of China, Hefei, 230026, China*

(Dated: January 26, 2024)

The striking discovery of high-temperature superconductivity (HTSC) of 80 K in a bilayer nickelate $La_3Ni_2O_7$ under a moderately high pressure of about 14 GPa ignited a new wave of studying HTSC in nickelates [1–9]. The properties of the parental phase at ambient pressure may contain key information on basic interactions therein and bosons that may mediate pairing giving birth to superconductivity. Moreover, the bilayer structure of $La_3Ni_2O_7$ may suggest a distinct minimal model in comparison to cuprate superconductors. Here using X-ray absorption spectroscopy and resonant inelastic X-ray scattering, we studied $La_3Ni_2O_7$ at ambient pressure, and found that Ni $3d_{x^2-y^2}$, Ni $3d_{z^2}$, and ligand oxygen $2p$ orbitals dominate the low-energy physics with a small charge-transfer energy. Remarkably, well-defined optical-like magnetic excitations were found to soften into a quasi-static spin-density-wave ordering, evidencing the strong electronic correlations and rich magnetic properties. Based on a Heisenberg spin model, we found that the inter-layer effective magnetic superexchange interaction is much larger than the intra-layer ones, and proposed viable magnetic structures. Our results highlight that the strong bonding of Ni $3d_{z^2}$ orbitals within the bilayer structure induces novel electronic and magnetic excitations setting the stage for further exploration of $La_3Ni_2O_7$ superconductor.

Introduction

Unlike cuprate superconductors, often characterized by a single Zhang-Rice singlet band consisting of Cu $3d_{x^2-y^2}$ and O $2p$ orbitals, multiple d orbitals and Ni-O bilayer structure play critical roles in $La_3Ni_2O_7$ [1, 2, 5, 10–13]. In particular, the molecular bonding between the two Ni $3d_{z^2}$ orbitals through the apical O p_z orbital, together with Ni $3d_{x^2-y^2}$ orbital, is widely established by theory and deemed as an essential ingredient for the low-energy electronic structure of $La_3Ni_2O_7$ [2, 5, 8, 13–16]. However, the exact orbital occupancy and orbital character of $La_3Ni_2O_7$ remains elusive. If $La_3Ni_2O_7$ is viewed in close proximity to cuprates, *i.e.*, at the limit of a small charge-transfer energy, significant amount of electron holes would occupy the oxygen ligands, giving rise to Zhang-Rice-like physics [17]. On the other hand, supposing it was a sibling of infinite-layer nickelate superconductors, where the charge-transfer energy is rather comparable to the Coulomb repulsion, the participation of the oxygen ligands in the low-energy electronic structure would be much reduced [18–20].

The bilayer structure and the multi-orbital nature of $La_3Ni_2O_7$ have profound impact on its magnetism as well, which plays a pivotal role in theories on this novel superconductor, resembling the cuprate case [1, 5, 21, 22]. Some suggest the importance of the interlayer antiferromagnetic coupling J_z between d_{z^2} orbitals [1, 5]; some others advocate that the strong interlayer coupling would cause the bilayer splitting of band structure, while in-plane magnetic exchange interactions play a dominant role in superconductivity [12, 14]. The intricate magnetic exchange may as well lead to other exotic phases with broken symmetries that have complex interplay with superconductivity, as seen in the cuprate superconductors [23, 24]. In the as-grown $La_3Ni_2O_7$ crystal at ambient pressure, resistivity measurements have found a kink-like transition at around 153 K, which responds to the external out-of-plane magnetic field, implying a possible spin-density-wave (SDW) therein [25]. A recent μSR experiment on polycrystalline $La_3Ni_2O_7$ suggested that a static long-range magnetic order emerges below 148 K, consistent with an SDW internal field distribution [26]. Moreover, traces of a possible density wave have been discovered in a latest NMR report [27]. However, the exact nature of this density-wave state

* Equal contributions
† yilu@nju.edu.cn
‡ kejin.zhou@diamond.ac.uk
§ dlfeng@ustc.edu.cn

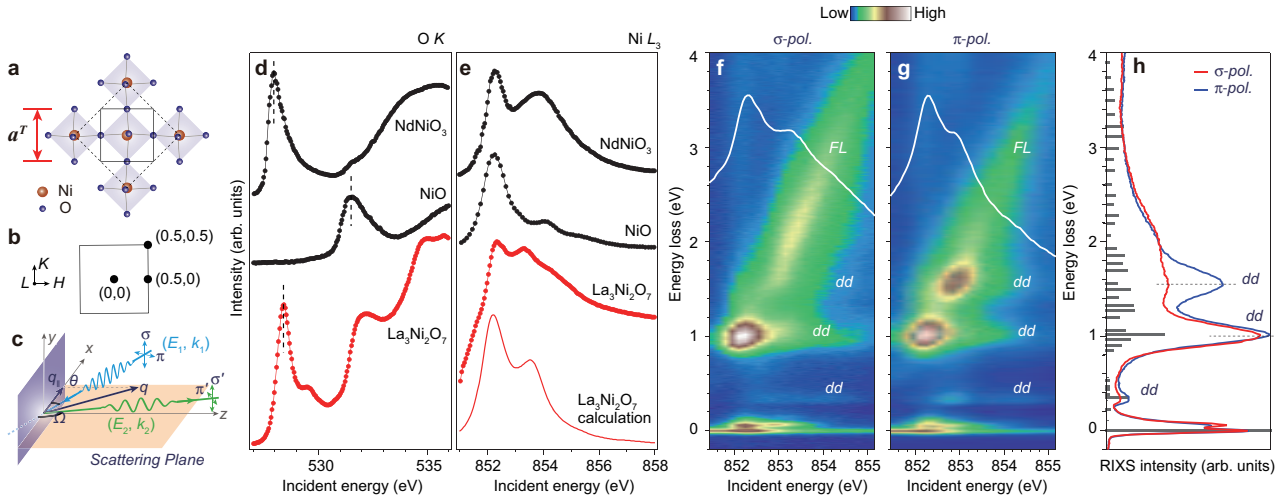

FIG. 1. **XAS spectra and the incident energy dependent RIXS maps in $La_3Ni_2O_7$. a,** Schematic top view of the NiO_2 plane in $La_3Ni_2O_7$. The solid black square represents the pseudo-tetragonal unit cell with a lattice constant $a^T \sim 3.833$ Å, while the dashed black square represents the real orthorhombic in-plane unit cell when considering the tilting of Ni-O octahedra. **b,** In-plane Brillouin zone (BZ) for the pseudo-tetragonal unit cell. **c,** Sketch of the RIXS experimental geometry. Details of the setup are described in Method. **d,e,** σ polarised XAS spectra of $La_3Ni_2O_7$ (red filled circles) taken at the O K-edge (d) and Ni L_3-edge (e), respectively. The latter is displayed after subtracting the background of La M_4-edge. The calculated Ni L_3-XAS (red curve) is also displayed. XAS spectra measured on NiO (Ni^{2+}) and $NdNiO_3$ (Ni^{3+}) (black-filled circles) are shown as references. **f,g,** RIXS intensity maps measured as a function of incident photon energy with σ- (f) and π-polarized photons. (g), respectively. The corresponding XAS spectrum is superimposed as a solid white curve on each map. Both XAS and RIXS spectra were collected at 20 K at a grazing-in incident angle of 20°. **h,** Integral of RIXS spectra in (f) and (g) over the incident energy range [851.8 eV, 853.4 eV]. The grey solid bars display the multiplet calculations for the Ni L_3-RIXS.

is still unclear.

Given the currently limited knowledge on the essential electronic and magnetic energy scales, such as the charge-transfer gap and exchange interactions, experimental verification is indispensable. In this work, we employ X-ray absorption spectroscopy (XAS) and resonant inelastic X-ray scattering (RIXS) at both Ni L_3-edge and O K-edge of $La_3Ni_2O_7$ single crystal at ambient pressure. These spectroscopic and scattering techniques are sensitive to low-energy electronic and magnetic structures together with elementary excitations, and thus they are ideally suited for tackling the core issues in $La_3Ni_2O_7$.

Electronic structure of $La_3Ni_2O_7$

As-grown $La_3Ni_2O_7$ crystallizes in an orthorhombic structure with the space group of *Amam* [1]. We define the reciprocal space index (H, K, L) based on the pseudo-tetragonal unit cell (Figs. 1a and 1b, Method). Figure 1c shows the experimental geometry, in which the incident X-ray is linearly polarised, while the scattered X-ray is typically non-polarised but otherwise polarised if stated explicitly (see Method).

Figures 1d and 1e illustrate XAS spectra of $La_3Ni_2O_7$ taken near the O K-edge and Ni L_3-edge, respectively. A sizable pre-edge peak at $\sim$ 528.5 eV is observed near the O K-edge, originating from oxygen $1s$ electron excitations into the unoccupied oxygen $2p$ ligand hole state near the Fermi level, as observed for the Zhang-Rice singlet state in cuprate superconductors [28]. The Ni L_3-XAS data show a sharp resonant peak around 852.4 eV, followed by a broad satellite peak at a higher energy. As the Ni valence 2.5+ of $La_3Ni_2O_7$ falls in between the archetypal nickelates NiO and $NdNiO_3$, the XAS spectra of $La_3Ni_2O_7$ can be qualitatively understood in relation to these two. NiO is a canonical charge-transfer insulator in the Zaanen-Sawatzky-Allen classification, whose large charge-transfer energy Δ ($\approx$ 5 eV) suppresses the charge fluctuations between the Ni $3d$ and ligand oxygen $2p$ orbitals despite their large orbital hopping integral [29]. Consequently, its ground state is well described by $\alpha|3d^8\rangle + \beta|3d^9\underline{L}\rangle$ ($\alpha^2 + \beta^2 \lesssim 1$ and $\underline{L}$ denotes a ligand hole) with a dominant $3d^8$ character ($\alpha^2 \approx 0.8$) [30–33]. On the other hand, the perovskite $NdNiO_3$ with a nominal $3d^7$ configuration is widely acknowledged as a negative charge-transfer system, where electrons from ligand oxygen spontaneously transfer onto Ni cations, resulting in a ground state with a leading $3d^8\underline{L}$ contribution [34]. Such a substantial ligand hole concentration is underscored by the pronounced pre-edge hole peak in the O K-edge XAS of $NdNiO_3$, similar to that of $La_3Ni_2O_7$ (Fig. 1d). This is distinct from NiO, where the pre-peak is absent, and the unoccupied ligand states are at an elevated energy across the charge-transfer gap. For the Ni L_3-XAS, the prominent resonant peak of $La_3Ni_2O_7$ is also observed for NiO and $NdNiO_3$ at a similar energy (Fig. 1e), which was previously identified as the Ni $2p \rightarrow 3d^8$ or $3d^8 + 3d^8\underline{L}$ transitions into the half-filled e_g states, respectively [34, 35]. A broad satellite peak at a higher energy is likewise seen for $NdNiO_3$, originating mainly from a part of its ground state wavefunction that contains additional ligand holes [34, 36, 37]. The above spectral features at both the O K-edge and Ni L_3-edge indicate a predominant $3d^8$ occupancy on the Ni cation in $La_3Ni_2O_7$, accompanied by significant amount of ligand holes.

Figures 1f and 1g show the incident-energy dependent RIXS measurements of $La_3Ni_2O_7$ across the Ni L_3-edge. A clear low-energy excitation ($\sim$ 70 meV) is observed near the elastic peak which will be discussed in the next section. The sharp XAS resonance at $\sim$ 852.4 eV decays mainly to a final state of a localized excitation at around 1 eV, known as the $t_{2g} \rightarrow e_g$ *dd* orbital excitation similar to NiO and $NdNiO_3$ [36, 38, 39]. The band-like fluorescence excitation, decaying from the broad satellite XAS peak, stems from the delocalized Ni-O hybridized continuum states [36, 37]. The intensity distribution of the fluorescence contracts under π polarization that couples stronger to the $3d_{z^2}$ orbital, indicative of a smaller out-of-plane bandwidth arising from the quasi-two-dimensional structure. In addition, distinct from $NdNiO_3$, two extra *dd* excitations show up in $La_3Ni_2O_7$ (at around 0.4 eV and 1.6 eV). They exhibit stronger intensities under π polarization, suggesting a more prominent involvement of the $3d_{z^2}$ orbital in them.

To gain a quantitative understanding of XAS and RIXS measurements, we built a double-cluster model capturing the bilayer structure of $La_3Ni_2O_7$ and then carried out multiplet calculations for Ni L_3- XAS and RIXS spectra (see details in Section 2 of Supplementary Information). Systematic optimizations of the calculated spectra suggest that the charge-transfer energy Δ falls between 0 and 2 eV, pointing out the rather small-charge-transfer nature of $La_3Ni_2O_7$ [40]. This result is reasonable since Δ is $\sim$ 5 eV and $\sim$ 0 for NiO and $NdNiO_3$, respectively [37, 41]. With the estimated range of Δ, the ground state wavefunction of $La_3Ni_2O_7$ can be deduced to approximately $\alpha|3d^8\rangle + \beta|3d^8\underline{L}\rangle + \gamma|3d^7\rangle$ with leading α^2 and β^2. The calculated XAS for Δ = 0.5 eV is shown in Fig. 1e, which corresponds to a ground state with $(\alpha^2, \beta^2, \gamma^2)$ $\approx$ (0.4, 0.3, 0.2). The corresponding RIXS calculation agrees well with the experiment, showing *dd* excitations identified at comparable energies (Fig. 1h). Notably, we found that both the XAS line shape and the lower *dd* excitation ($\sim$ 0.4 eV) in RIXS show marked difference upon tuning the inter-layer hopping strength mediated by the $3d_{z^2}$ -O_{AP} $2p_z$ - $3d_{z^2}$ orbital overlap in the calculation (O_{AP} stands for the apical oxygen), underlining the importance of the inter-layer coupling for the electronic structure (Section 2 of Supplementary Information). This result is consistent with previous experimental report [1], and lends support to several recent theoretical works emphasizing on the importance of the bilayer structure [2, 5, 13–15, 42–45].

Magnetic excitations

Figure 2 summarises the detailed energy-momentum dependence of low-energy excitations in $La_3Ni_2O_7$ taken at the incident energy of 852.4 eV corresponding to the resonance peak of Ni L_3-XAS. Figures 2a and 2b show strongly dispersive excitations along directions illustrated in insets. The excitations reach maximal energy of about 70 meV at (0, 0) and (0.5, 0) while soften to zero energy (within the experimental energy resolution) at (0.25, 0.25), suggesting the presence of a quasi-static order. Similar excitations also appear when excited by π incident X-rays polarisation (Fig. S6). Along the out-of-plane direction, this mode does not exhibit sizable dispersion as a function of L, indicating its quasi-two-dimensional nature (Fig. 2c).

As both magnon and phonon excitations could appear in RIXS spectra, particularly within 100 meV that is closely relevant to both, the polarimetric RIXS was employed to analyze the outgoing X-rays linear polarisation for unraveling the origin of these excitations (see Methods). Clearly, as shown in Fig. 2d, the inelastic excitation is present under the $\pi - \pi'$, $\pi - \sigma'$, and $\sigma - \pi'$ channels, while gets much reduced under the $\sigma - \sigma'$ channel. Such behaviour is in excellent agreement with the assumption of a magnetic origin of the scattering [46]. Our multiplet RIXS calculation of magnetic excitations in the double-cluster model confirmed the outgoing polarisation dependence (Fig. S5). Concerning phonons, in principle, their spectra weight should be present in the $\sigma-\sigma'$ channel. However, the corresponding polarimetric RIXS spectrum shows negligible spectral weight hence a minute contribution to the Ni L_3-RIXS (Fig. 2d). We therefore conclude that the low-energy excitations observed at the Ni L_3-edge are dominated by magnons. This immediately infers a quasi-static SDW order at (0.25, 0.25). Remarkably, an SDW order was reported to exist near (0.25, 0.25) in the half-doped nickelate $La_{3/2}Sr_{1/2}NiO_4$, which has the same nominal $Ni^{2.5+}$ valence state as that of $La_3Ni_2O_7$ [47]. In both cases, the magnon softens to almost zero energy near the SDW ordering wavevector, while their dispersions approaching Γ point deviate drastically: there is an acoustic-like magnon in $La_{3/2}Sr_{1/2}NiO_4$, whereas it is absent here in Fig. 2a.

By fitting the magnon spectra to a damped harmonic oscillator (DHO) function $\chi''(q, \omega)$, we extracted the peak energy and width of the magnon (Section 4 of Supplementary Information) [48]. Three possible spin configurations consistent with the spin order at $Q = (0.25, 0.25)$ can be constructed: the diagonal spin-charge stripe order as in half-doped $La_{3/2}Sr_{1/2}NiO_4$ where Ni^{2+} spin and nominal Ni^{3+} charge stripes intertwined (Stripe-1, Fig. 3a) [47]; the SDW order could also be realised without the charge inhomogeneity, *i.e.*, a double-spin stripe order (Stripe-2, Fig. 3b) that is similar to the bi-collinear spin order in FeTe [49]; by exchanging the Stripe-1 charge stripe positions with those of a spin stripe, a third spin configuration could be achieved as a double spin-charge stripe order (Stripe-3 in Fig. S10c). For all these SDW orders, owing to the strong bilayer bonding, spins are antiferromagnetically aligned in the top and bottom NiO_2 layers. To obtain the magnetic superexchange interaction parameters, we constructed an effective J_1-J_2-J_z Heisenberg model: $H = \sum_i J_z \vec{S}_i^t \cdot \vec{S}_i^b + \sum_{\langle ij\rangle\alpha} J_1 \vec{S}_i^\alpha \cdot \vec{S}_j^\alpha + \sum_{\langle\langle ij\rangle\rangle\alpha} J_2 \vec{S}_i^\alpha \cdot \vec{S}_j^\alpha$, where α is the layer index for the bottom (b) or top (t) layer. J_z is the inter-layer exchange coupling along the c-axis. J_1 and J_2 are the nearest-neighbor and next-nearest-neighbor exchange couplings, respectively, in a single NiO_2 layer. The magnon dispersion within the linear spin wave theory was solved using the torque equation formalism [50] (Section 6 of Supplementary Information). We found that the magnon dispersion based on both Stripe-1 and Stripe-2 spin configurations agree with our RIXS result (Fig. 3c and Section 6 of Supplementary Information). Owing to the scattering matrix effect, the simulated acoustic magnon spectra are significantly

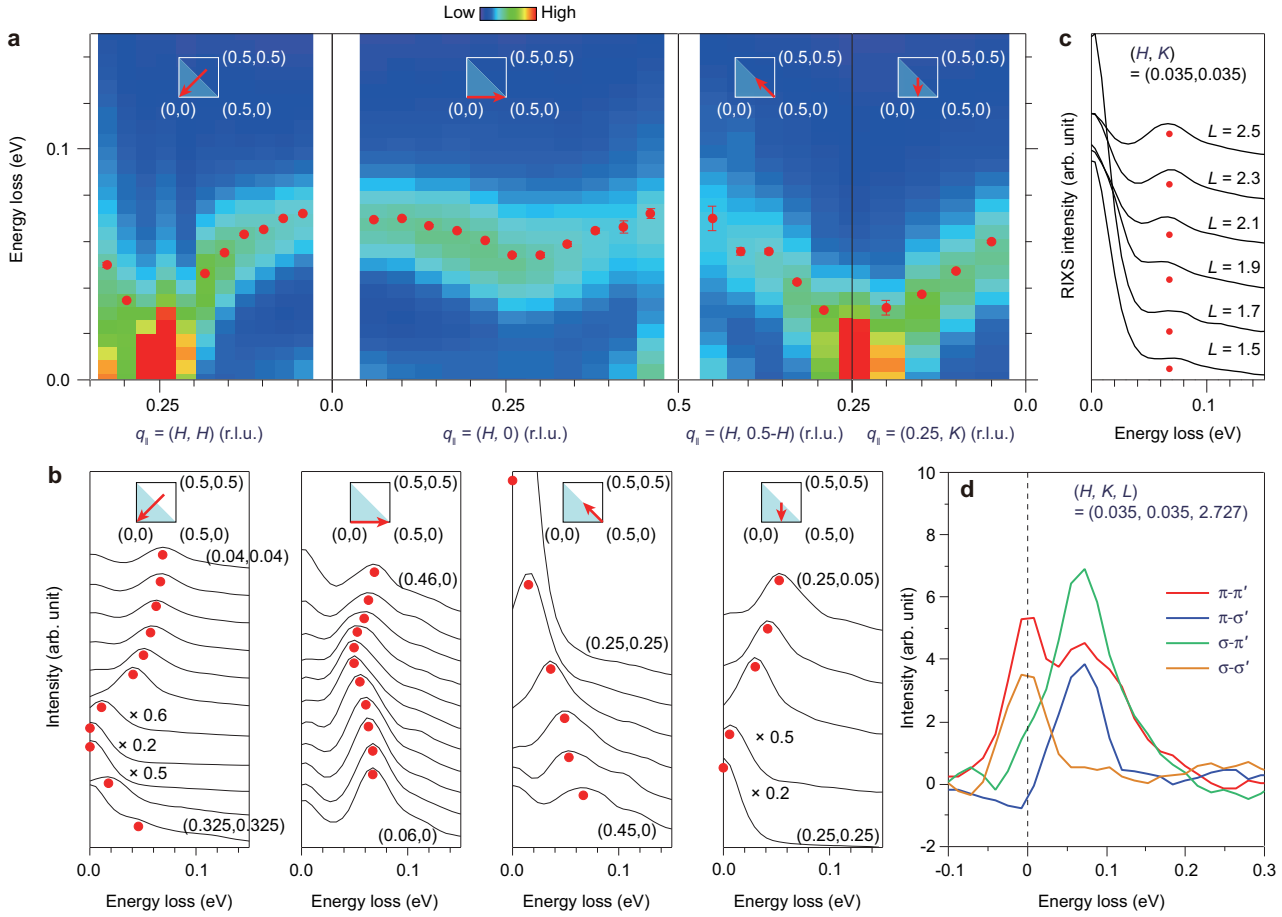

FIG. 2. **Energy-momentum dependent magnon in $La_3Ni_2O_7$. a,** RIXS intensity maps along high-symmetry directions as indicated in the insets. Data were collected at 20 K using 852.4 eV, σ-polarised X-ray at the Ni L_3-edge. The red circles depict the peak positions of magnetic excitations here and throughout all panels of this figure. **b,** RIXS spectra at representative projected in-plane momentum transfers. The weaker excitations at ~120 meV may result from the multi-magnons. **c,** L scan of RIXS spectra at at $q_{\parallel}$ = (0.035, 0.035). **d,** Polarimetric RIXS data at q = (0.035, 0.035, 2.727). The spectra are decomposed into $\pi - \pi'$, $\pi - \sigma'$, $\sigma - \sigma'$ and $\sigma - \pi'$ components.

weaker than the optical magnon, consistent with the experimental findings. In general, the inter-layer effective superexchange interaction is an order of magnitude larger than that of the intra-layer. The finding of a dominant magnetic interaction along the molecular bonding direction is in good accordance with previous theoretical calculation [2]. Interestingly, the J_2S here shows comparable strength to that in the half-doped $La_{3/2}Sr_{1/2}NiO_4$ [47]. On the other hand, the weak J_1 coupling in Stripe-2 leads the similar spin dynamic equations and magnon dispersions to Stripe-1. Based on the above results and the currently limited information, we can conjecture the true spin configuration of $La_3Ni_2O_7$ is either Stripe-1 or Stripe-2 or their mixture (see details in Section 5 of Supplementary Information).

Spin-density-wave order

We then took an explicit examination on the SDW order. Polarimetric RIXS was used to confirm the magnetic origin of low-energy excitations, likewise, it was applied to characterize this SDW order in $La_3Ni_2O_7$. Similar to the behaviour of magnons, the momentum-dependent quasi-elastic SDW scattering peak shows the same trend, *i.e.*, sizable scattering intensities under $\pi - \pi'$, $\pi - \sigma'$, and $\sigma - \pi'$ except for $\sigma - \sigma'$ (Figs. 4a and 4b), confirming the magnetic origin of such SDW order. Further insight into the nature of the SDW was gained through the energy dependence of the SDW scattering at its order wavevector across the Ni L_3-edge (Fig. 4c). Unlike the XAS spectra where La M_4 shows a greater absorption intensity than that of Ni L_3, the SDW scattering predominantly results from the Ni $3d$ - O $2p$ hybridised states. Furthermore, the SDW scattering peak exhibits a colossal polarisation dependence, namely, its intensity probed under π polarisation is about 30 times higher than that with σ polarisation. Figure 4d gives an example taken with 852.4 eV photons, which may indicate its strong association with Ni $3d_{z^2}$ orbital. The half-width at half-maximum Γ = 0.0022±0.0002 r.l.u. of the scattering peak corresponds to a relatively short in-plane correlation length ($\xi_H = 1/\Gamma$) of ~27.7 nm. A much broader peak is observed as a function of L along the direction of (0.25, 0.25, L) establishing the quasi-two-dimensional nature of such SDW order (Fig. 4e).

The temperature dependence of the SDW order illustrates

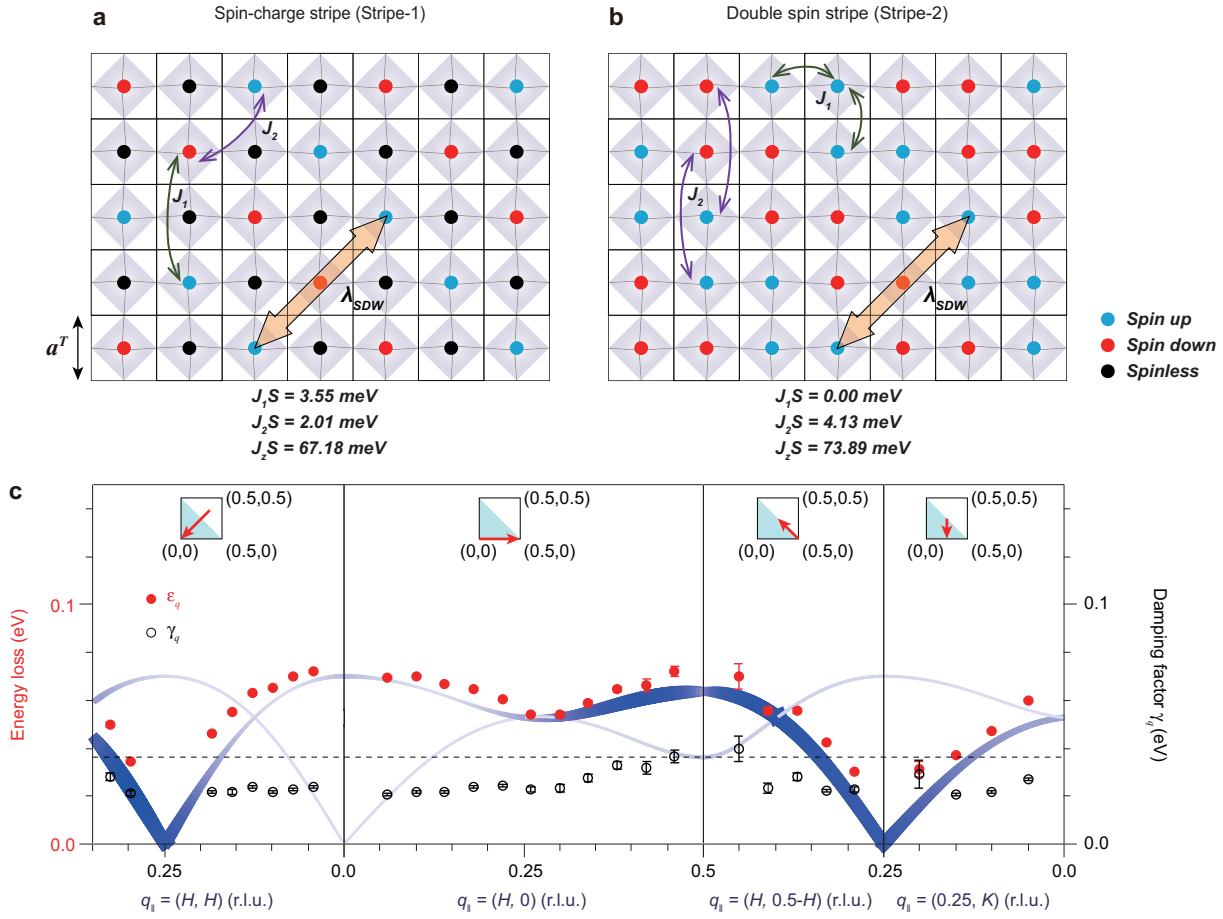

FIG. 3. **The spin configuration and the magnon dispersion of $La_3Ni_2O_7$ a,** The spin configurations for the spin-charge stripe order (Stripe-1). To simplify the sketch only nickel cations are shown. The blue, red and black circles represent spin up Ni^{2+}, spin down Ni^{2+}, and the nominal Ni^{3+} sites, respectively. The solid lines illustrate the in-plane pseudo-tetragonal unit cells and the grey cubics represent the Ni-O octahedra. The fitted values of J_1S, J_2S, and J_zS based on this spin configuration are noted (see details in Section 6 of Supplementary Information). **b,** The spin configuration for the double spin stripe (Stripe-2), and the fitted value of J_1S, J_2S, and J_zS. **c,** The experimental magnon dispersion ϵ_q (red filled circles) and damping factor γ_q (black open circles) versus projected in-plane momentum transfer $q_\parallel$ along high-symmetry directions at 20 K. See fitting details in Section 4 of Supplementary Information. Error bars of ϵ_q were estimated by combining the uncertainty of the elastic peak position, linear background, and the standard deviation of the fits. Error bars of γ_q were estimated by combining the standard deviation of the fits. The horizontal dashed line marks the total energy resolution (36 meV). The results of an effective J_1-J_2-J_z Heisenberg model based on Stripe-1 order are overlaid. The results from the model based on Stripe-2 are also consistent to the experimental data. The blue curves represent the dispersion of two magnon modes, where the thickness of the lines and the depth of their color represent the mode intensity. The detailed parameters are listed in Section 6 of Supplementary Information.

a substantial reduction in both the intensity and the correlation length when the temperature is raised above ~150 K (Figs. 4f-4h). While the SDW wavevector does not exhibit a discernible temperature dependence (Fig. 4i). The discovery of the SDW with a characteristic temperature of around 150 K agrees well with previous transport, NMR and μSR measurements on $La_3Ni_2O_7$ [25–27].

Discussion and Conclusion

Our RIXS and XAS measurements revealed the dispersive magnon and SDW order below 150 K in $La_3Ni_2O_7$. Detailed analysis suggests that Ni $3d_{x^2-y^2}$, Ni $3d_{z^2}$, and O $2p$ orbitals dominate the low-energy physics with charge-transfer energy less than 2 eV, and the inter-layer effective magnetic superexchange interaction is much larger than the intra-layer ones. These give critical information for constructing the minimal model for $La_3Ni_2O_7$ superconductor.

Apart from the extraordinary bilayer structure and the associated predominant magnetic exchange interaction, the electronic structure of $La_3Ni_2O_7$ fits in general into the family of Ruddlesden-Popper (RP) nickelates. The formation of the Zhang-Rice-like hole band, the small charge-transfer energy, and the well-defined dispersive magnon allude to its nature of the strong electronic correlations [51]. The above are typical characteristics of the strongly correlated cuprates where charge- and spin-density modulation can take place. Moreover, the occurrence of SDW order at (0.25, 0.25) is reminiscent of that in the half-doped single-layer $La_{3/2}Sr_{1/2}NiO_4$,

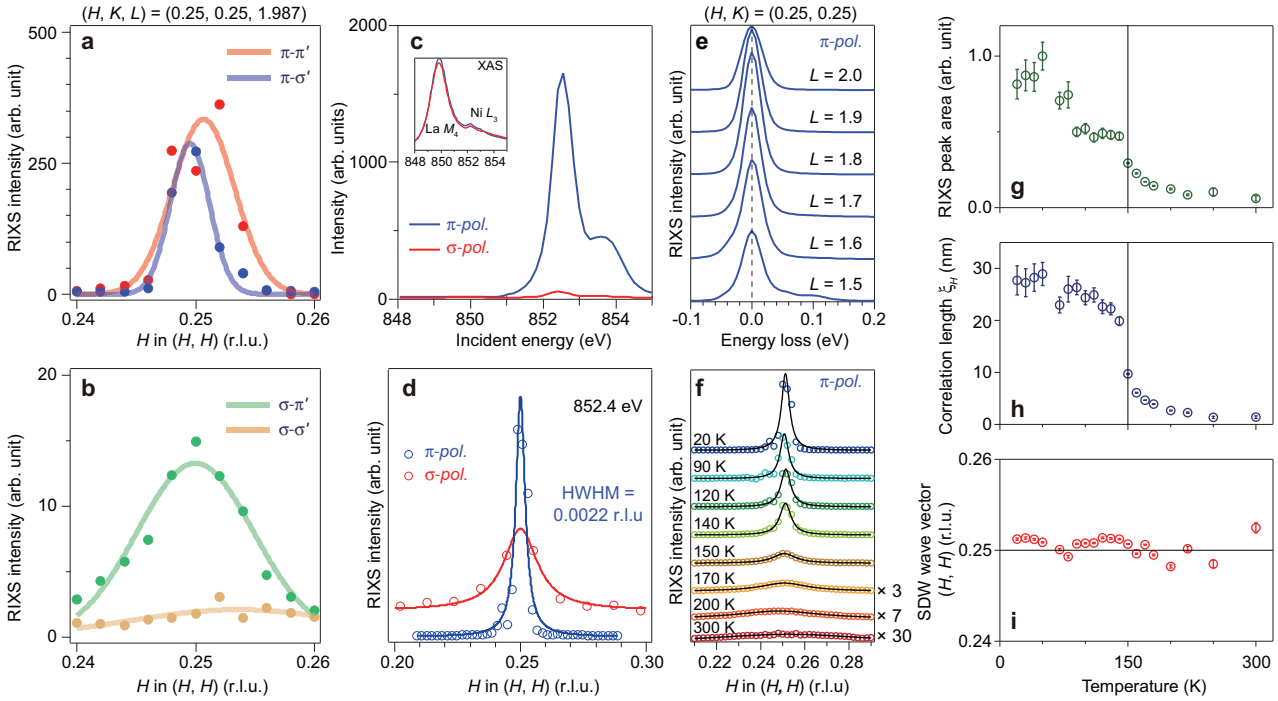

FIG. 4. **SDW order at (0.25, 0.25) of $La_3Ni_2O_7$.** **a,b** Polarimetric RIXS data. The spectra are decomposed into $\pi\pi'$, $\pi\sigma'$, $\sigma\sigma'$ and $\sigma\pi'$ components. **c,** SDW peaks intensities as a function of incident photon energy and polarization. The inset shows the XAS spectra at the La M_4-edge and the Ni L_3-edge. **d,** SDW peak intensity integrated over an energy window of 36.5 meV (the total energy resolution) as a function of projected momentum transfer ($q_\parallel$) along the (H, H) direction. The fitted peak center values are $\sim$ 0.25 r.l.u. and the corresponding half width at the half maximum (HWHM) is 0.0022 r.l.u. **e,** L scan of RIXS spectra at $q_\parallel$ = (0.25,0.25). **f,** SDW peaks and their Lorentzian fits along the (H, H) direction at various temperatures. **g-i,** Temperature dependence of the SDW peak area (g), the correlation length (h) and the SDW wave vector position (i).

where a spin-charge stripe order exists, and implies the tendency to a charge-density-wave instability in $La_3Ni_2O_7$ as illustrated in the scenario of Stripe-1 (Fig.3a) [40, 47]. Indeed in layered half-doped RP nickelates, manganites, and cobaltates, the spin-charge intertwined order is prevailing [47, 52, 53]. On the other hand, the double spin stripe order accommodating homogeneous charge-density (Stripe-2, Fig. 3b) may be possible too as the $3d_{x^2-y^2}$ orbitals are more itinerant in-plane than the $3d_{z^2}$ orbitals. Verifying the existence and the extent of the charge-density-wave order could help elucidate which picture of the spin configuration $La_3Ni_2O_7$ is closer to.

Finally, we would like to extrapolate our findings to superconducting $La_3Ni_2O_7$, here, a moderately high pressure induces a structural phase transition accompanied by a few percent shrinkage of the lattice constants, and the Ni-O-Ni bonding angles between adjacent NiO_6 octahedra straighten to 180° [1]. Consequently, the electronic hopping is likely to increase, potentially suppressing density waves that compete with the superconductivity [54, 55]. Furthermore, the magnetic superexchange J_z may get significantly enlarged due to the increased hopping along Ni-O_{AP}-Ni. Despite the presence of Zhang-Rice singlet physics and competing orders as in cuprates, the reinforced molecular orbital bonding and the dominating inter-layer AFM interaction may be novel additions to the HTSC of such a bilayer nickelate superconductor.

ACKNOWLEDGMENTS

This work was supported by National Natural Science Foundation of China (Nos.11888101, U2032208, 12274207, 12174428, and 12174454), the New Cornerstone Science Foundation, and the National Key R&D Program of China (Nos. 2023YFA1406304, 2022YFA1403000, 2023YFA1406500, and 2023YFA1406002). We acknowledge Diamond Light Source for providing beamtime at I21 Beamline under Proposal MM35805 and the science commissioning beamtime for using the polarimeter at I21. Work at SYSU was as well supported by the Guangdong Basic and Applied Basic Research Funds (No. 2021B1515120015), Guangzhou Basic and Applied Basic Research Funds (Nos. 202201011123, 2024A04J6417), and Guangdong Provincial Key Laboratory of Magnetoelectric Physics and Devices (No. 2022B1212010008).

[1] Sun, H. *et al.* Signatures of superconductivity near 80 K in a nickelate under high pressure. *Nature* **621**, 493–498 (2023).

[2] Luo, Z., Hu, X., Wang, M., Wú, W. & Yao, D.-X. Bilayer two-

orbital model of $La_3Ni_2O_7$ under pressure. *Phys. Rev. Lett.* **131**, 126001 (2023).

[3] Christiansson, V., Petocchi, F. & Werner, P. Correlated electronic structure of $La_3Ni_2O_7$ under pressure. *Phys. Rev. Lett.* **131**, 206501 (2023).

[4] Yang, S. *et al.* Effective Bi-Layer Model Hamiltonian and Density-Matrix Renormalization Group Study for the High-T_c Superconductivity in $La_3Ni_2O_7$ under High Pressure. *Chinese Physics Letters* **40**, 127401 (2023).

[5] Liu, Y. B., Mei, J. W., Ye, F., Chen, W. Q. & Yang, F. $s^{\pm}$ wave pairing and the destructive role of apical-oxygen deficiencies in $La_3Ni_2O_7$ under pressure. *Phys. Rev. Lett.* **131**, 236002 (2023).

[6] Zhang, Y. *et al.* High-temperature superconductivity with zero-resistance and strange metal behavior in $La_3Ni_2O_7$. *arXiv preprint arXiv:2307.14819* (2023).

[7] Zhang, Y., Lin, L.-F., Moreo, A., Maier, T. A. & Dagotto, E. Structural phase transition, $s_{\pm}$-wave pairing and magnetic stripe order in the bilayered nickelate superconductor $La_3Ni_2O_7$ under pressure. *arXiv preprint arXiv:2307.15276* (2023).

[8] Yang, J. *et al.* Orbital-dependent electron correlation in double-layer nickelate $La_3Ni_2O_7$. *arXiv preprint arXiv:2309.01148* (2023).

[9] Hou, J. *et al.* Emergence of high-temperature superconducting phase in pressurized $La_3Ni_2O_7$ crystals. *Chinese Physics Letters* **40**, 117302 (2023).

[10] Lu, C., Pan, Z., Yang, F. & Wu, C. Interplay of two e_g orbitals in superconducting $La_3Ni_2O_7$ under pressure. *arXiv preprint arXiv:2310.02915* (2023).

[11] Kaneko, T., Sakakibara, H., Ochi, M. & Kuroki, K. Pair correlations in the two-orbital hubbard ladder: Implications on superconductivity in the bilayer nickelate. *arXiv preprint arXiv:2310.01952* (2023).

[12] Chen, J., Yang, F. & Li, W. Orbital-selective superconductivity in the pressurized bilayer nickelate $La_3Ni_2O_7$: An infinite projected entangled-pair state study. *arXiv preprint arXiv:2311.05491* (2023).

[13] Yang, Y.-f., Zhang, G.-M. & Zhang, F.-C. Interlayer valence bonds and two-component theory for high-T_c superconductivity of $La_3Ni_2O_7$ under pressure. *Phys. Rev. B* **108**, L201108 (2023).

[14] Tian, Y.-H., Chen, Y., Wang, J.-M., He, R.-Q. & Lu, Z.-Y. Correlation Effects and Concomitant Two-Orbital $s_{\pm}$-Wave Superconductivity in $La_3Ni_2O_7$ under High Pressure. *arXiv preprint arXiv:2308.09698* (2023).

[15] Dong, Z. *et al.* Visualization of oxygen vacancies and self-doped ligand holes in $La_3Ni_2O_{7-\delta}$. *arXiv preprint arXiv:2312.15727* (2023).

[16] Lechermann, F., Gondolf, J., Bötzel, S. & Eremin, I. M. Electronic correlations and superconducting instability in $La_3Ni_2O_7$ under high pressure. *Phys. Rev. B* **108**, L201121 (2023).

[17] Zhang, F. & Rice, T. Effective hamiltonian for the superconducting cu oxides. *Physical Review B* **37**, 3759 (1988).

[18] Lin, J. *et al.* Strong superexchange in a $d^{9-\delta}$ nickelate revealed by resonant inelastic X-ray scattering. *Phys. Rev. Lett.* **126**, 087001 (2021).

[19] Shen, Y. *et al.* Role of oxygen states in the low valence nickelate $La_4Ni_3O_8$. *Phys. Rev. X* **12**, 011055 (2022).

[20] Hepting, M. *et al.* Electronic structure of the parent compound of superconducting infinite-layer nickelates. *Nature materials* **19**, 381–385 (2020).

[21] Sachdev, S. Colloquium: Order and quantum phase transitions in the cuprate superconductors. *Rev. Mod. Phys.* **75**, 913–932 (2003).

[22] Zhang, Y., Lin, L.-F., Moreo, A. & Dagotto, E. Electronic structure, dimer physics, orbital-selective behavior, and magnetic tendencies in the bilayer nickelate superconductor $La_3Ni_2O_7$ under pressure. *Phys. Rev. B* **108**, L180510 (2023).

[23] Li, Y. *et al.* Unusual magnetic order in the pseudogap region of the superconductor $HgBa_2CuO_{4+\delta}$. *Nature* **455**, 372–375 (2008).

[24] Keimer, B., Kivelson, S. A., Norman, M. R., Uchida, S. & Zaanen, J. From quantum matter to high-temperature superconductivity in copper oxides. *Nature* **518**, 179–186 (2015).

[25] Liu, Z. *et al.* Evidence for charge and spin density waves in single crystals of $La_3Ni_2O_7$ and $La_3Ni_2O_6$. *Science China Physics, Mechanics & Astronomy* **66**, 217411 (2022).

[26] Chen, K. *et al.* Evidence of spin density waves in $La_3Ni_2O_{7-\delta}$. *arXiv preprint arXiv:2311.15717* (2023).

[27] Kakoi, M. *et al.* Multiband metallic ground state in multilayered nickelates $La_3Ni_2O_7$ and $La_4Ni_3O_{10}$ revealed by ^{139}La-NMR at ambient pressure. *arXiv preprint arXiv:2312.11844* (2023).

[28] Chen, C. T. *et al.* Electronic states in $La_{2-x}Sr_xCuO_{4+\delta}$ probed by soft-X-ray absorption. *Phys. Rev. Lett.* **66**, 104–107 (1991).

[29] Sawatzky, G. A. & Allen, J. W. Magnitude and origin of the band gap in NiO. *Phys. Rev. Lett.* **53**, 2339–2342 (1984).

[30] Medarde, M. *et al.* $RNiO_3$ perovskites (R= Pr, Nd): Nickel valence and the metal-insulator transition investigated by X-ray-absorption spectroscopy. *Phys. Rev. B* **46**, 14975 (1992).

[31] Mizokawa, T. *et al.* Electronic structure of $PrNiO_3$ studied by photoemission and X-ray-absorption spectroscopy: Band gap and orbital ordering. *Phys. Rev. B* **52**, 13865 (1995).

[32] Abbate, M. *et al.* Electronic structure and metal-insulator transition in $LaNiO_{3-\delta}$. *Phys. Rev. B* **65**, 155101 (2002).

[33] Horiba, K. *et al.* Electronic structure of $LaNiO_{3-x}$: An in situ soft X-ray photoemission and absorption study. *Phys. Rev. B* **76**, 155104 (2007).

[34] Green, R. J., Haverkort, M. W. & Sawatzky, G. A. Bond disproportionation and dynamical charge fluctuations in the perovskite rare-earth nickelates. *Phys. Rev. B* **94**, 195127 (2016).

[35] van der Laan, G., Zaanen, J., Sawatzky, G. A., Karnatak, R. & Esteva, J.-M. Comparison of x-ray absorption with x-ray photoemission of nickel dihalides and NiO. *Phys. Rev. B* **33**, 4253–4263 (1986).

[36] Bisogni, V. *et al.* Ground-state oxygen holes and the metal–insulator transition in the negative charge-transfer rare-earth nickelates. *Nat. Commun.* **7**, 13017 (2016).

[37] Lu, Y. *et al.* Site-selective probe of magnetic excitations in rare-earth nickelates using resonant inelastic X-ray scattering. *Phys. Rev. X* **8**, 031014 (2018).

[38] Chiuzbăian, S. G. *et al.* Localized electronic excitations in NiO studied with resonant inelastic X-ray scattering at the Ni *M* threshold: Evidence of spin flip. *Phys. Rev. Lett.* **95**, 197402 (2005).

[39] Nag, A. *et al.* Many-body physics of single and double spin-flip excitations in NiO. *Phys. Rev. Lett.* **124**, 067202 (2020).

[40] Chen, X., Jiang, P., Li, J., Zhong, Z. & Lu, Y. Critical charge and spin instabilities in superconducting $La_3Ni_2O_7$. *arXiv preprint arXiv:2307.07154* (2023).

[41] Tanaka, A. & Jo, T. Resonant 3*d*, 3*p* and 3*s* photoemission in transition metal oxides predicted at 2*p* threshold. *Journal of the Physical Society of Japan* **63**, 2788–2807 (1994).

[42] Jiang, K., Wang, Z. & Zhang, F.-C. High-temperature superconductivity in $La_3Ni_2O_7$. *Chinese Physics Letters* **41**, 017402 (2024).

[43] Qin, Q. & Yang, Y.-f. High-T_c superconductivity by mobilizing local spin singlets and possible route to higher T_c in pressurized $La_3Ni_2O_7$. *Phys. Rev. B* **108**, L140504 (2023).

[44] Qu, X.-Z. *et al.* Bilayer t-j-$j_{\perp}$ model and magnetically mediated

pairing in the pressurized nickelate $La_3Ni_2O_7$. *arXiv preprint arXiv:2307.16873* (2023).

[45] Lu, C., Pan, Z., Yang, F. & Wu, C. Interlayer coupling driven high-temperature superconductivity in $La_3Ni_2O_7$ under pressure. *arXiv preprint arXiv:2307.14965* (2023).

[46] Hill, J. & McMorrow, D. Resonant exchange scattering: polarization dependence and correlation function. *Acta Crystallographica Section A: Foundations of Crystallography* **52**, 236–244 (1996).

[47] Freeman, P. *et al.* Spin dynamics of half-doped $La_{3/2}Sr_{1/2}NiO_4$. *Phys. Rev. B* **71**, 174412 (2005).

[48] Peng, Y. *et al.* Dispersion, damping, and intensity of spin excitations in the monolayer (Bi, Pb)$_2$(Sr, La)$_2$$CuO_{6+\delta}$ cuprate superconductor family. *Physical Review B* **98**, 144507 (2018).

[49] Lipscombe, O. J. *et al.* Spin waves in the (π,0) magnetically ordered iron chalcogenide $Fe_{1.05}Te$. *Phys. Rev. Lett.* **106**, 057004 (2011).

[50] Carlson, E. W., Yao, D. X. & Campbell, D. K. Spin waves in striped phases. *Phys. Rev. B* **70**, 064505 (2004).

[51] Liu, Z. *et al.* Electronic correlations and energy gap in the bilayer nickelate $La_3Ni_2O_7$. *arXiv preprint arXiv:2307.02950* (2023).

[52] Sternlieb, B. *et al.* Charge and magnetic order in $La_{0.5}Sr_{1.5}MnO_4$. *Physical review letters* **76**, 2169 (1996).

[53] Zaliznyak, I., Hill, J., Tranquada, J., Erwin, R. & Moritomo, Y. Independent freezing of charge and spin dynamics in $La_{1.5}Sr_{0.5}CoO_4$. *Physical Review Letters* **85**, 4353 (2000).

[54] Souliou, S. M. *et al.* Rapid suppression of the charge density wave in $YBa_2Cu_3O_{6.6}$ under hydrostatic pressure. *Phys. Rev. B* **97**, 020503 (2018).

[55] Cyr-Choinière, O. *et al.* Sensitivity of T_c to pressure and magnetic field in the cuprate superconductor $YBa_2Cu_3O_y$: Evidence of charge-order suppression by pressure. *Phys. Rev. B* **98**, 064513 (2018).

[56] Zhou, K.-J. *et al.* I21: an advanced high-resolution resonant inelastic x-ray scattering beamline at diamond light source. *Journal of Synchrotron Radiation* **29**, 563–580 (2022).

[57] Cowan, R. D. *The Theory of Atomic Structure and Spectra* (Univ of California Press, 1981).

[58] Haverkort, M. W. Quanty for core level spectroscopy - excitons, resonances and band excitations in time and frequency domain. *J. Phys. Conf. Ser.* **712**, 012001 (2016).

[59] Kresse, G. & Furthmüller, J. Efficient iterative schemes for ab initio total-energy calculations using a plane-wave basis set. *Phys. Rev. B* **54**, 11169 (1996).

[60] Kresse, G. & Joubert, D. From ultrasoft pseudopotentials to the projector augmented-wave method. *Phys. Rev. B* **59**, 1758 (1999).

[61] Perdew, J. P., Burke, K. & Ernzerhof, M. Generalized gradient approximation made simple. *Phys. Rev. Lett.* **77**, 3865 (1996).

[62] Wang, V., Xu, N., Liu, J.-C., Tang, G. & Geng, W.-T. Vaspkit: A user-friendly interface facilitating high-throughput computing and analysis using vasp code. *Computer Physics Communications* **267**, 108033 (2021).

[63] Dudarev, S. L., Botton, G. A., Savrasov, S. Y., Humphreys, C. & Sutton, A. P. Electron-energy-loss spectra and the structural stability of nickel oxide: An LSDA+ U study. *Phys. Rev. B* **57**, 1505 (1998).

[64] Haverkort, M. W. Theory of resonant inelastic X-ray scattering by collective magnetic excitations. *Phys. Rev. Lett.* **105**, 167404 (2010).

Methods

Sample fabrication: $La_3Ni_2O_7$ sample was fabricated by the high oxygen pressure floating zone technique and the details are described in [25]. The sample quality was checked by X-ray diffraction (XRD) and Laue diffraction (see details in Fig. S1). Samples were cleaved to get a flat, clean surface before RIXS measurements.

XAS and RIXS measurements: XAS and RIXS measurements were performed at Beamline I21 at Diamond Light Source [56]. In this work, we describe the structural properties of $La_3Ni_2O_7$ referencing to a pseudo-tetragonal unit cell with cell parameters $a^T = b^T \sim 3.833$ Å and $c = 20.45$ Å. Reciprocal lattice units (r.l.u.) are defined (where $2\pi/a^T = 2\pi/b^T = 2\pi/c = 1$) with $\mathbf{Q} = H\mathbf{a}^{T*} + K\mathbf{b}^{T*} + L\mathbf{c}^*$. The crystallographic a^T–c (b^T–c) plane of $La_3Ni_2O_7$ single crystal was aligned within the horizontal scattering plane (Fig. 1c). The polar angular offsets (θ and χ) of the crystal were aligned by the (002) diffraction peak, and the azimuthal offset (ϕ) by SDW order peak, such that the c^* axis lays in the scattering plane. The spectrometer arm was at a fixed position of $\Omega = 154°$ except for L scans where variable Ω was employed.

XAS spectra were collected with a grazing incidence angle of $\theta_0 = 20°$ to probe both in-plane and out-of-plane unoccupied states. All XAS measurements were done at a temperature of 20 K with the exit slit opening to 30 μm. Total electron yield XAS spectra were collected using the draincurrent and normalised to the incoming beam intensity. Both linear vertical (σ) and horizontal (π) polarisations were used.

Energy-dependent RIXS measurements were performed at the grazing incidence angle of $\theta_0 = 20°$ and the temperature of 20 K. The exit slit was open to 30 μm corresponding to an average energy resolution of 40 meV (FWHM). The incident energy range went from 851 to 855 eV in steps of 0.2 eV to fully capture the resonance behaviour across the Ni-L_3 absorption peaks.

Momentum-dependent RIXS measurements were performed at the resonant energy of 852.4 eV at a temperature of 20 K with the exit slit opening to 20 μm corresponding to an average energy resolution of 36 meV (FWHM). RIXS spectra were collected using both σ and π polarisations. The grazing out geometry ($\theta > \Omega/2$) was applied for the acquisition of RIXS spectra shown in the main text.

Polarimetric RIXS apparatus employs a graded multilayer designed for the Ni L_3-edge with a grazing incidence angle of 20° lying perpendicular to the scattering plane. Measurements were performed at Q = (0.035, 0.035, L) and around (0.25, 0.25, L) to analyse the outgoing X-rays linear polarisation of the magnon and SDW ordering, respectively. The total energy resolution of the polarimetric RIXS is ~ 55 meV (FWHM). Since the multilayer does not work at the exact Brewster's angle, the outgoing polarised RIXS (the indirect RIXS) from the reflection of the multilayer will be a mixture of linearly polarised spectra. The direct and indirect RIXS spectral intensities are then given by the following formula:

$$I_{direct} = I_{\sigma'} + I_{\pi'} \quad (1)$$

$$I_{indirect} = R_{\sigma'} I_{\sigma'} + R_{\pi'} I_{\pi'} \quad (2)$$

where I_{direct} and $I_{indirect}$ stands for the outgoing nonpolarised and mixed polarised RIXS spectral intensity, respectively. From the above formula, the outgoing σ' and π' polarised RIXS spectra can be deduced:

$$I_{\pi'} = \frac{I_{indirect} - R_{\sigma'} I_{direct}}{R_{\pi'} - R_{\sigma'}} \quad (3)$$

$$I_{\sigma'} = \frac{I_{indirect} - R_{\pi'} I_{direct}}{R_{\sigma'} - R_{\pi'}} \quad (4)$$

In the above, $R_{\sigma'}$ ($R_{\pi'}$) refers to the multilayer reflectivity of the outgoing σ' (π') polarised X-ray photon. At the Ni L_3-edge, $R_{\sigma'}$ and $R_{\pi'}$ is 14.1% and 9.1%, respectively, based on the calibration of the multilayer.

Theoretical calculations: The Ni L_3-edge XAS and RIXS calculations shown in Figure 1 were performed employing a fully correlated Ni_2O_{11} cluster model, accounting for the two corner-sharing NiO_6 octahedra within the pseudo-tetragonal unit cell. The noninteracting part of the Hamiltonian integrates material-specific on-site energies and hybridizations involving Ni $3d$ and O $2p$ orbitals, along with spin-orbit coupling within the Ni core $2p$ and $3d$ shells. Full Coulomb interactions within the Ni $3d$ shell and between the Ni $2p$ and $3d$ shells are included, with parametrization by Slater integrals scaled at 0.8 based on atomic Hartree-Fock values [57]. Comprehensive details regarding model construction and relevant parameters are described in Section 2 of Supplementary Information. The model was solved using the exact diagonalization method as implemented in Quanty [58].

The DFT calculations employ the Vienna ab-initio simulation package (VASP) code [59] with the projector augmented wave (PAW) method [60]. The Perdew-Burke-Ernzerhof (PBE) exchange-correlation functional [61] is used. The energy cutoff energy for expanding the wave functions into a plane-wave basis is set to be 500 eV. The Γ-centered k-mesh is used in KPOINTS files which are generated by VASPKIT [62] with the KPT-resolved value equal to 0.02 for different unit cells. The SDW orders are calculated using the simplified rotation invariant approach based on the DFT+U method introduced by Dudarev *et al*. [63]. Then, the effective Heisenberg interactions for the SDW orders are constructed. The magnon dispersion within the linear spin wave theory are calculated using the torque equation formalism[18, 50]. The RIXS intensity for the magnon mode in the σ-π polarization channel is calculated following the reference [64]. More details can be found in Sections 5 and 6 of Supplementary Information.

Author contributions

J.C., X.Y.C., D.W.S., S.A., M.G.-F., D.L.F., and K.-J.Z. conducted XAS and RIXS experiments at Diamond Light Source. X.Y.C., S.A., J.C., and K.-J.Z. analyzed the data. J.M., K.J., and J.P.H. performed DFT and stripe states calculations. J.L. and Y.L. performed multiplet calculations. H.L.S., X.H., and M.W. fabricated samples. X.Y.C. and Z.C.J. performed XRD and Laue measurements. K.-J.Z., K.J., Y.L., D.W.S., D.L.F., and X.Y.C. wrote the manuscript, with input from all authors. D.L.F. and K.-J.Z. are responsible for project direction and planning.

Competing interests

Authors declare that they have no competing interests.

Data availability

All data are available in the main text and Supplementary Information.

Supplementary Files

This is a list of supplementary files associated with this preprint. Click to download.

- La3Ni2O7RIXSSIfinal.pdf